universe

Article

Frequency Shift of Electromagnetic Radiation Around Charged Hayward Black Hole

Bakhodirkhon Saidov [1], Bakhtiyor Narzilloev [2,3,4,5], Ahmadjon Abdujabbarov [2,6,7], Malika Khudoyberdieva [2] and Bobomurat Ahmedov [1,2,8,*]

[1] Institute of Fundamental and Applied Research, National Research University TIIAME, Kori Niyoziy 39, Tashkent 100000, Uzbekistan; saidbaxodirxon13@gmail.com
[2] Ulugh Beg Astronomical Institute, Astronomy Str. 33, Tashkent 100052, Uzbekistan; baxtiyor@astrin.uz (B.N.); ahmadjon@astrin.uz (A.A.); xudoyberdiyeva94@inbox.ru (M.K.)
[3] Department of Mathematics, University of Tashkent for Applied Sciences, Str. Gavhar 1, Tashkent 100149, Uzbekistan
[4] Shahrisabz State Pedagogical Institute, Shahrisabz Str. 10, Shahrisabz 181301, Uzbekistan
[5] Institute of Engineering Physics, Samarkand State University, University Avenue 15, Samarkand 140104, Uzbekistan
[6] Power Engineering Faculty, Tashkent State Technical University, Tashkent 100095, Uzbekistan
[7] Institute of Nuclear Physics, Ulugbek 1, Tashkent 100214, Uzbekistan
[8] Department of Physics, New Uzbekistan University, Movarounnahr Str. 1, Tashkent 100000, Uzbekistan
* Correspondence: ahmedov@astrin.uz

Abstract: In this work, we investigate spacetime and photon dynamics around a charged Hayward black hole, focusing on the effects of electric charge Q and the length factor l. Our analysis shows that the maximum charge for black hole existence decreases as l increases, vanishing at $l/M \simeq 0.77$. The black hole has both inner and outer horizons, with the outer horizon shrinking and the inner horizon expanding as spacetime parameters increase. The spacetime curvature, measured by the Kretschmann scalar, is most pronounced when both parameters are small, resembling the Schwarzschild black hole. The electric charge strongly influences the curvature and photon sphere size, while the effect of the length factor is less significant. Additionally, the gravitational redshift of photons is more sensitive to the electric charge of the compact object than the length factor, diminishing as Q increases and with greater radial distance from the black hole. Overall, while both spacetime parameters affect black hole properties, the electric charge has a slightly stronger impact, especially on gravitational redshift and photon behavior.

Keywords: black hole; general relativity; redshift of photons; photon sphere

PACS: 04.20.-q; 04.50.+h; 04.70.-s; 04.70.Bw; 04.50.-h

Citation: Saidov, B.; Narzilloev, B.; Abdujabbarov, A.; Khudoyberdieva, M.; Ahmedov, B. Frequency Shift of Electromagnetic Radiation Around Charged Hayward Black Hole. *Universe* **2024**, *10*, 454. https://doi.org/10.3390/universe10120454

Academic Editor: Aharon Davidson

Received: 29 October 2024
Revised: 1 December 2024
Accepted: 7 December 2024
Published: 12 December 2024

1. Introduction

The famous singularity theorem states that under certain conditions, the gravitational collapse of sufficiently massive stars will inevitably result in the formation of spacetime singularities [1–7]. One major issue in classical general relativity is the unavoidable presence of these singularities. The standard black hole solutions, such as the Schwarzschild, Reissner–Nordström, and Kerr metrics, all contain curvature singularities within their interiors. This has led to the view that classical general relativity requires modifications where spacetime curvature becomes infinite, and that these singularities might be resolved by quantum gravity. However, since there is no fully developed theory of quantum gravity, efforts to address the singularity inside black holes have turned toward regular models, which are inspired by quantum principles. Regular black holes typically associated with classical black hole solutions, have garnered significant attention as viable extensions of general relativity. These objects are characterized by modifications to the traditional

Schwarzschild or Kerr spacetimes, often implemented through effective metrics inspired by quantum gravity, nonlinear electrodynamics, or gravitational decoupling techniques. Recent works, such as those exploring atemporality in Lorentzian–Euclidean black holes, have highlighted the role of these models in addressing singularity issues in both static and dynamic spacetimes [8]. Comprehensive reviews, including [9], provide a detailed summary of the advancements in the field, emphasizing their theoretical foundations and astrophysical implications. The dynamics around these regular black holes, particularly the behavior of geodesics, have been extensively studied. For instance, the analysis of geodesic motion in Euclidean Schwarzschild geometry offers insights into nonsingular black hole metrics [10]. Additionally, studies utilizing gravitational decoupling methods have explored both the spacetime structure and thermodynamic properties of these solutions, shedding light on their stability and horizon characteristics [11]. It has been suggested by Sakharov [12] and Gliner [13] that for small values of r, the Einstein tensor takes the form $G_{\mu\nu} = \Lambda g_{\mu\nu}$ with $\Lambda \neq 0$, meaning there is a central de Sitter core that follows the equation of state $P = -\rho$. This condition effectively places an upper limit on the scalar curvature. As a result, the collapsed object reaches a metastable state, where the outward de Sitter pressure counteracts the inward gravitational pull, eliminating the curvature singularity at the center. In the presence of a horizon, this leads to what is known as a regular black hole. Bardeen [14] first implemented this concept to create a model for a regular black hole, which was later shown to be an exact solution of Einstein's field equations coupled with nonlinear electrodynamics (NED) [15–17]. Since then, many other regular black hole models have been developed and explored [18–23] (see [24] for a comprehensive review). The lack of central singularities makes challenges like Hawking radiation and the information loss paradox less severe [25]. Hayward [26] subsequently introduced a model that is particularly useful for studying the collapse and evaporation processes, describing the formation of a black hole from a vacuum as a regular black hole, which can also be derived within the NED framework. When coupled with electric charge, the Hayward black hole becomes a rich ground for exploring the interplay between spacetime geometry and electromagnetic fields in a regular black hole setting. It is worth noting that there are several ways to investigate the given spacetime around black holes. For example, in our previous research, we have extensively investigated various spacetime metrics around compact objects, utilizing several different methodologies [27–38]. Particle motion around modified Hayward black holes has been extensively studied in various works, including [26,39–44]. These studies provide insights into the geodesic structure and associated dynamical phenomena in such spacetimes. Additionally, the shadow cast and weak gravitational lensing effects around electrically charged Hayward black holes have been analyzed in detail in [45].

In this work, we investigate the properties of spacetime around a charged Hayward black hole through photon dynamics, focusing on the impact of both the electric charge and the length factor. We examine how these parameters affect the horizon structure, spacetime curvature, photon sphere size, and gravitational redshift of photons. The work may be interesting due to the following reasons. The detailed analysis of the iron K_α emission line in the accretion disk of a black hole is a powerful tool for constraining the parameters of the central black hole. The iron line is emitted when iron atoms in the accretion disk are ionized by X-ray photons and then transition back to lower energy states, producing characteristic photons with an energy of approximately 6.4 keV [46,47]. Due to the strong gravitational field near the black hole, the emitted line profile is modified by relativistic Doppler effects caused by the disk's orbital motion, gravitational redshift due to the black hole's gravity, and light bending influenced by the curvature of spacetime near the black hole [48,49]. The resulting line is broadened and asymmetric, with a red wing extending to lower energies, shaped by gravitational redshift and Doppler shifts, and a blue peak at higher energies, dominated by emissions from the approaching side of the disk [50]. The shape of this line encodes critical information about the geometry and dynamics of the accretion disk, as well as the properties of the black hole. The inner edge of the accretion disk, defined by the innermost stable circular orbit (ISCO), depends on the black hole's spacetime parameters.

For example, in the case of the Kerr black hole, a more extended red wing indicates a smaller ISCO, corresponding to higher values of spin [51]. Additionally, the gravitational redshift and Doppler broadening depend on the black hole's mass. By combining iron line analysis with other observations, such as X-ray luminosity or variability timescales, it is possible to estimate key black hole parameters [52]. Observational data from X-ray observatories like XMM-Newton, NuSTAR, or Chandra are modeled using relativistic line profiles [53,54]. Models such as RELXILL [54] and KYRLINE [55] simulate the expected iron line shape based on black hole and disk parameters. Advanced simulations trace photons from the accretion disk to the observer, incorporating all relevant relativistic effects, including gravitational lensing and redshift [56]. These simulations refine parameter estimation by accounting for the complex geometry of the system. Iron line analysis is often complemented by other methods to constrain black hole properties. The continuum fitting method uses the thermal emission from the accretion disk to estimate the black hole's spin [57], while quasi-periodic oscillations (QPOs) offer additional constraints on the black hole's mass, spin, and other parameters [58].

The work is organized in the following way: In Section 2, we provide a brief introduction to the spacetime metric of the electrically charged Hayward black hole and examine its basic properties. In Section 3, we solve the equations of motion for photons orbiting the central black hole. Section 4 outlines the steps for calculating the gravitational redshift of photons, and the main findings of the work are discussed in Section 5.

Geometrized units ($G = c = 1$) have been selected in the work. Greek indices can take values $\alpha = 0, 1, 2, 3$, and the spacetime signature is chosen to be (−,+,+,+).

2. Spacetime of Charged Nonrotating Hayward Black Hole

The metric for the electrically charged Hayward black hole (CHBH) is expressed as follows [59]

$$ds^2 = -\left(1 - \frac{(2Mr - Q^2)r^2}{r^4 + (2Mr + Q^2)l^2}\right)dt^2 + \left(1 - \frac{(2Mr - Q^2)r^2}{r^4 + (2Mr + Q^2)l^2}\right)^{-1} dr^2 + r^2 d\theta^2 + r^2 \sin^2\theta d\phi^2. \tag{1}$$

In this expression, Q represents the electric charge of a black hole, M denotes its mass, and l is a length parameter that is related to the magnetic charge by the relation $g^3 = 2Ml^2$. It can be verified that as the length parameter approaches zero ($l \to 0$), the metric reduces to the Reissner–Nordström solution. The radial profile of the lapse function, which can be defined as

$$f(r) = 1 - \frac{(2Mr - Q^2)r^2}{r^4 + (2Mr + Q^2)l^2},$$

is illustrated in Figure 1. The left panel shows a fixed length parameter with varying electric charge, while the right panel shows a fixed electric charge with varying length parameters. Both parameters (Q and l) exhibit almost identical effects, and at asymptotic infinity, the metric approaches flat Minkowski spacetime. Additionally, increasing either Q or l enlarges the metric function $f(r)$ near the black hole, while at larger distances, their effects become insignificant.

The location of the event horizon can be easily determined from the condition $g^{rr} = 0$. However, it is important to note that an event horizon does not exist for all the values of the spacetime parameters l and Q. In Figure 2, we display the parameter space, clearly distinguishing between black hole and non-black-hole regions, separated by the blue solid line. From the figure, it is evident that in the absence of l, the maximum absolute value of the electric charge for a black hole is $Q_{max} = M$, as in the case of the Reissner–Nordström black hole. When l is present, however, the maximum allowed electric charge for which a black hole solution still exists decreases, approaching zero as l/M approaches approximately 0.77.

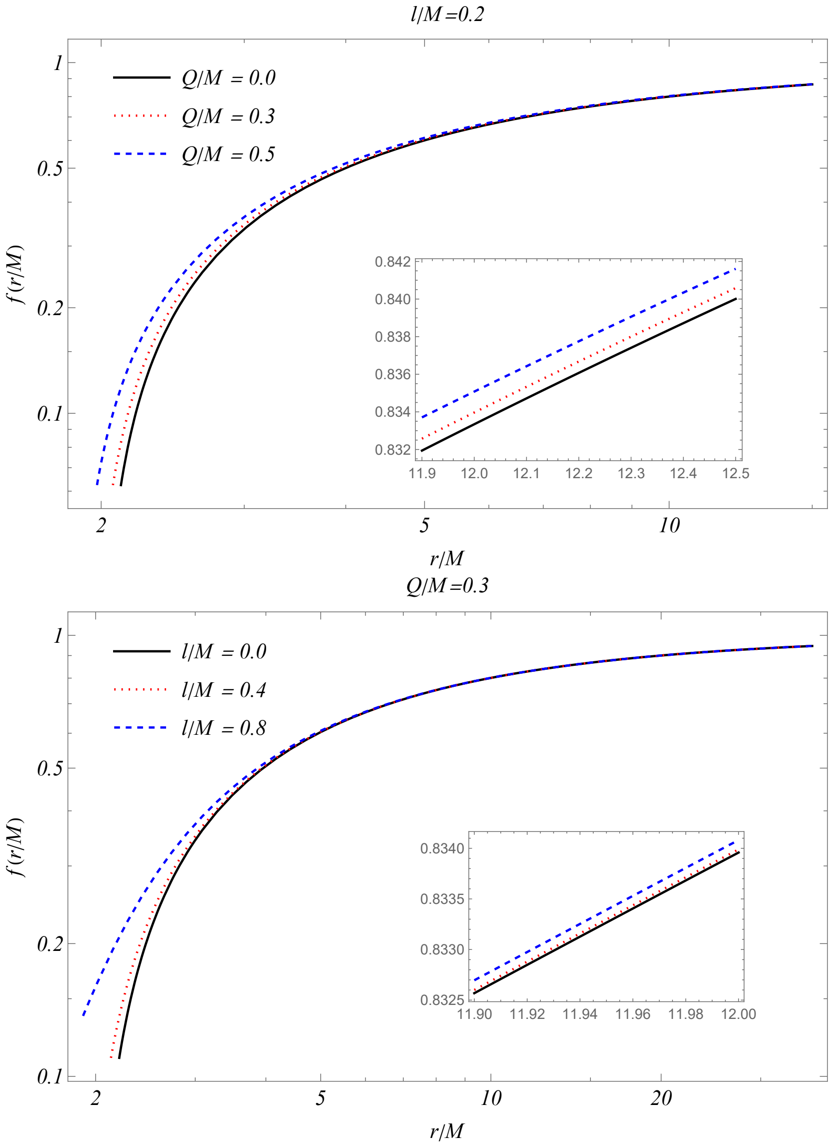

Figure 1. Radial dependence of lapse function of charged Hayward black hole with spacetime parameters are fixed.

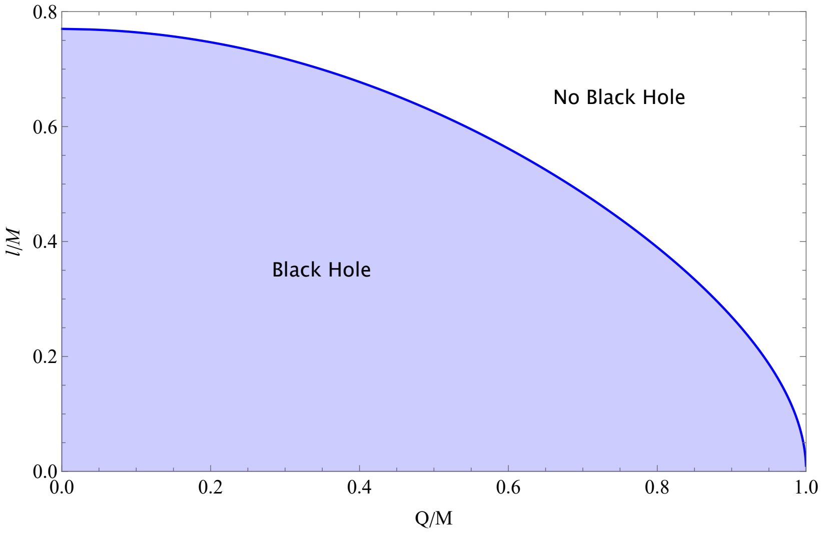

Figure 2. Black hole/non-black-hole regions in the parameter space of l–Q.

We can now directly solve $g^{rr} = 0$ to determine the event horizon's location, as given in Figure 3. The figure clearly shows that in general, the given black hole solution possesses two horizons, namely, the inner horizon and outer event horizon which can meet with the inner one at some specific values of spacetime parameters l and Q. It is clear that increasing both parameters reduces the event horizon size in a similar manner while increasing the inner horizon. The plots also demonstrate that an increase in one spacetime parameter reduces the maximum value of the second to have a black hole solution, as discussed previously.

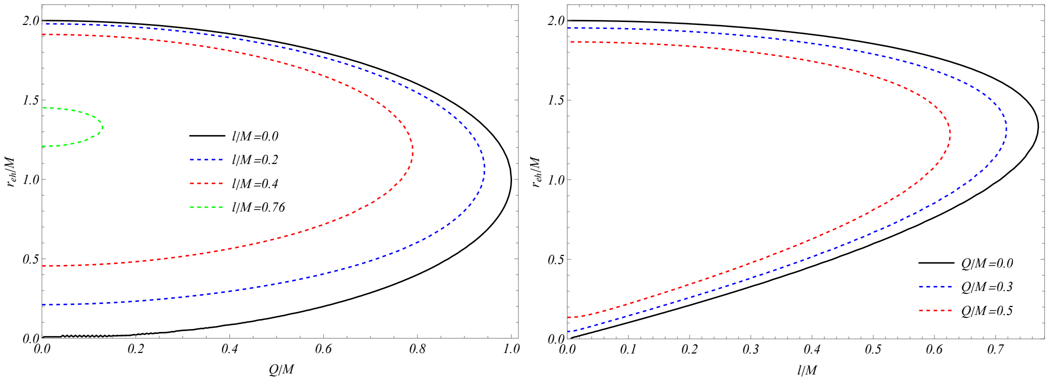

Figure 3. The event horizon radius of the photon that is dependent on spacetime parameters of charge and length.

To check whether the found locations are indeed coordinate singularities (at which $g_{rr} \to \infty$) but not physical singularities, one can analyze the behavior of so-called Kretschmann scalar $K = R^{\alpha\beta\mu\nu}R_{\alpha\beta\mu\nu}$ (with $R_{\alpha\beta\mu\nu}$ being Riemann tensor), which is a coordinate-independent quantity. One can see how the Kretschmann scalar behaves with the change in radial coordinate, as presented in Figure 4. In the top-left panel, the effect of the electric charge of a black hole for fixed l is shown, and in the right one, the effect of l for fixed Q is shown. From the top-left panel, one can see that the effect of the electric charge strongly depends on the radial coordinate inside a black hole. One can see that it is not monotonic everywhere near the center. But one thing is clear, in the presence of the length factor, the given black hole solution is regular always. The top-right panel demonstrates a similar effect from the length factor for the fixed value of the electric charge of a black hole. One noticeable point is that when $l = 0$, the given solution involves physical singularity, since it recovers the Reissner–Nordström solution. In the middle left panel, we show a density plot version of the dependence of the Kretschmann scalar from spacetime parameters for the fixed radial distance inside a black hole (since the outside is predictable). It clearly shows that the curvature of spacetime is not monotonic everywhere. For example, when both spacetime parameters tend to zero, one can notice that the curvature of spacetime starts increasing. One can also see that smaller values of l and bigger values of Q also cause the curvature of spacetime inside a black hole to increase, and in a faster manner as compared with the previous case. But one should take into account that the given statements are true for the selected radial distance. In the middle-right panel, the density plot version of the dependence of the Kretschmann scalar with the change in radial coordinate and electric charge of a black hole for fixed l is shown. It is noticeable that the behavior of the Kretschmann scalar becomes monotonic starting from distances $r \gtrsim 0.5M$. As expected, the curvature starts increasing very fast when the given solution tends to Schwarzschild case $l \to 0$, $Q \to 0$. In the bottom plot, how the Kretschmann scalar for fixed electric charge changes with the change in the radial coordinate and length factor l is demonstrated. In the density plot, we see that in general, smaller values of l and closer distance to the center result in bigger values of Kretschmann scalar.

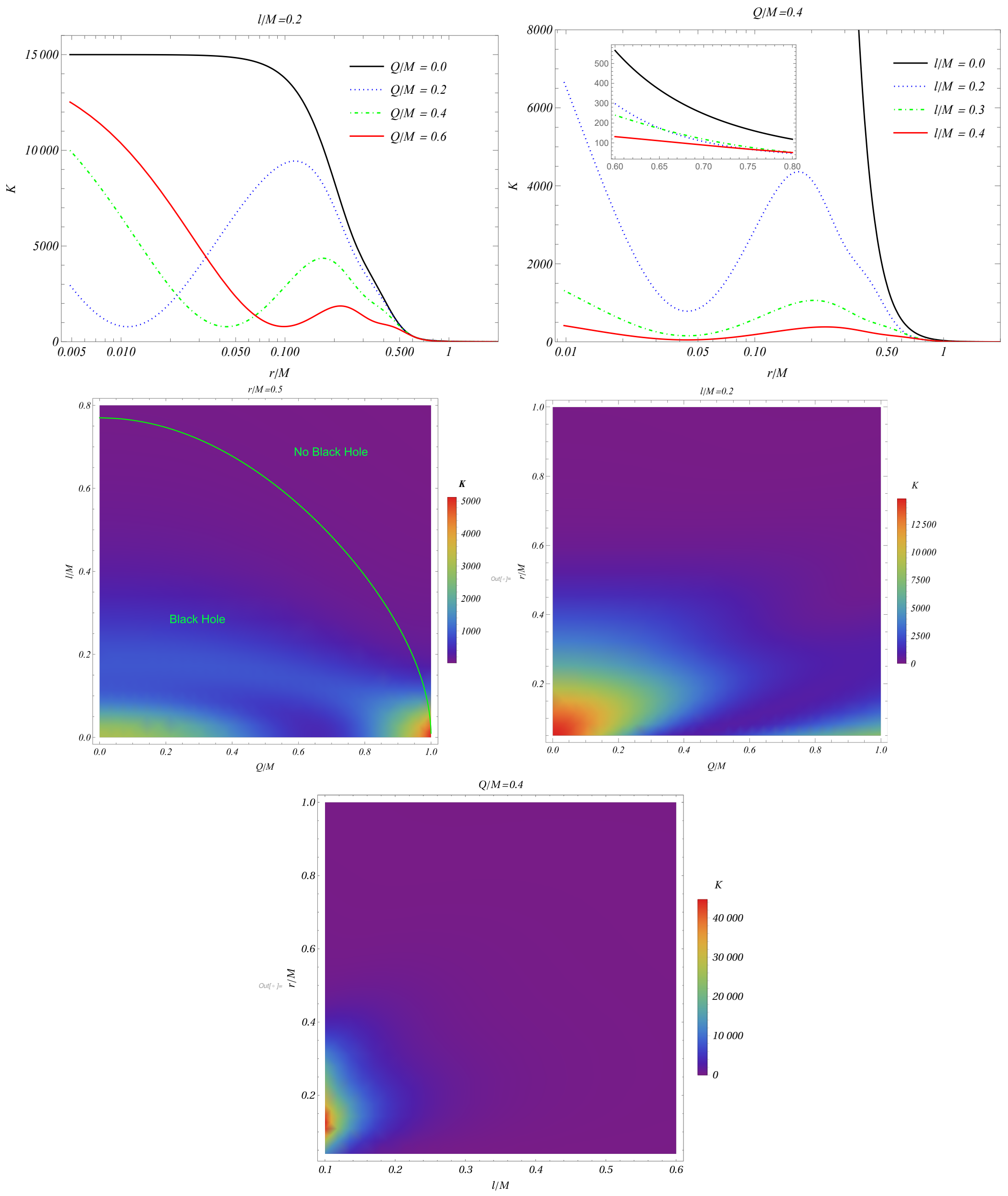

Figure 4. The change in Kretschmann scalar with the change in the radial coordinate and spacetime parameters.

3. Photon Motion

In this section, we study the motion of photons in the spacetime of CHBH. One way to do so is by using Hamilton–Jacobi formalism for the given spacetime. The equation of motion reads as

$$g^{\mu\nu}\frac{\partial S}{\partial x^{\mu}}\frac{\partial S}{\partial x^{\nu}} = 0, \tag{2}$$

where S defines the action and x^{μ} coordinates of photons. If we assume photons are moving on the equatorial plane, then the action can be written in the form

$$\mathcal{S} = -E_{\gamma}t + L_{\gamma}\phi + \mathcal{S}_r + \mathcal{S}_{\theta} \tag{3}$$

where E_{γ} and L_{γ} are conserved quantities of a photon which refer to its energy and angular momentum, respectively. Since the spacetime is spherically symmetric, photons that begin their motion on the equatorial plane will remain confined to that plane, which allows one to take $\dot{\theta} = 0$. Then, one can easily solve the Hamilton–Jacobi equation with respect to $\dot{r}$, which in turn allows one to take the effective potential of photons as

$$V_{eff}(r) = -E_\gamma^2 \left[1 - \frac{(2Mr - Q^2)r^2}{r^4 + (2Mr + Q^2)l^2}\right]^{-1} - \frac{L_\gamma^2}{r^2}. \tag{4}$$

One can plot the change of the effective potential with the change of distance from the central compact object for different values of spacetime parameters Q and l, as shown in Figure 5. The left panel of the figure shows that the more electric charge a black hole has, the weaker the effective potential of photons becomes. But, this is noticeable only near the central compact object, and at further distances, the effect of the electric charge quickly approaches zero. Similar behavior of the effective potential can be observed in the right panel of Figure 5, which is for the fixed electric charge of a black hole and different values of length parameter l. One noticeable difference is that the effect of the latter decreases faster as compared with the effect of the electric charge with the increase in the distance from the central compact object.

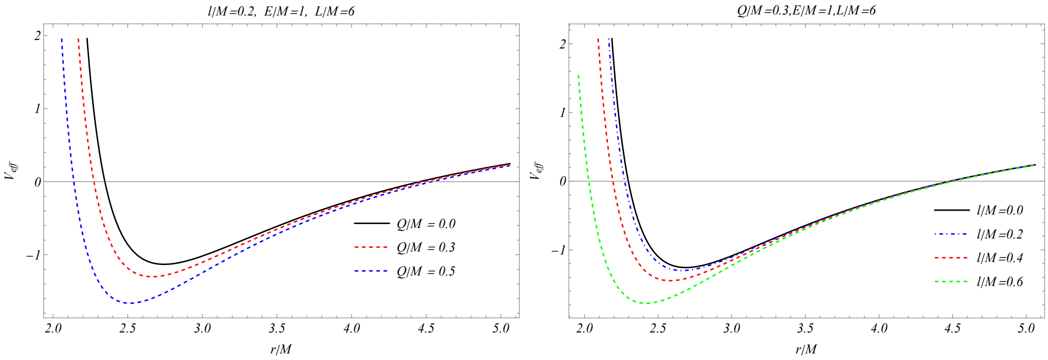

Figure 5. The radial dependence of effective potential of photons moving around charged Hayward black hole.

One of the distinct features of black holes is that, due to their extreme gravitational field, they can have a region in their close vicinity called a photon sphere. The photon sphere is a spherical region around a black hole where gravitational forces are strong enough to cause photons to follow circular orbits. It represents the boundary at which light can orbit the black hole due to the curvature of spacetime. In Schwarzschild black holes, the photon sphere is located at a radius of $r = 3M$. For rotating black holes, such as Kerr black holes, the photon sphere becomes more complex, with different radii depending on the photon's direction of motion (co-rotating or counter-rotating with respect to the black hole's spin). Since our spacetime solution is spherically symmetric, the photon sphere is spherical in shape with a specific radius. The photon sphere is significant because it marks the closest distance at which light can orbit the black hole stably. Any light that passes within this sphere either falls into the black hole or escapes to infinity, but it cannot maintain a circular orbit. One can use the effective potential of photons to obtain the radius of such photon sphere for the charged Hayward black hole using the following conditions:

$$V_{eff}(r) = 0, \qquad V'_{eff}(r) = 0 \tag{5}$$

where prime $(')$ denotes the derivative with respect to r. The results are shown in Figure 6. From the left panel, we observe that an increase in the electric charge of a black hole decreases the size of the photon sphere, and an increase in the length factor shifts the lines towards a smaller radius of the photon sphere. The right panel demonstrates that the length factor demonstrates similar behavior as the electric charge, but its effect is considerably lower compared with the electric charge.

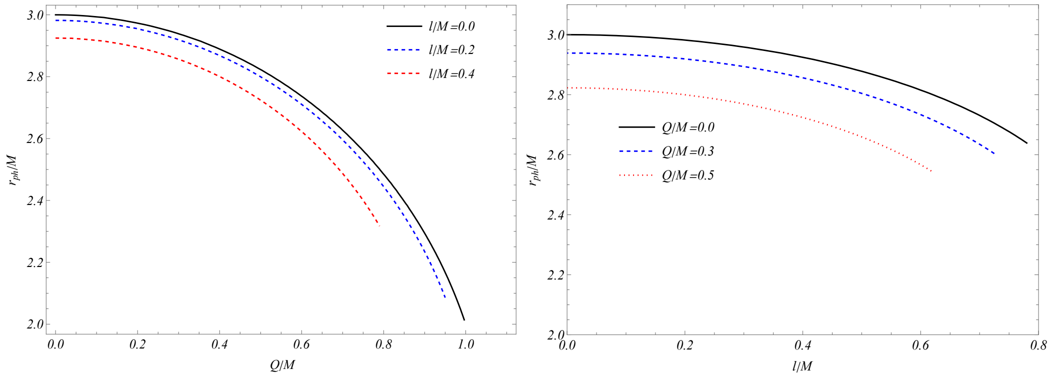

Figure 6. Influence of spacetime parameters on the photon sphere radius.

4. Gravitational Redshift of Photons

In this work, we employ the Herrera–Nucamendi (HN) method [60] to analyze the redshift and blueshift of photons emitted by particles orbiting a central black hole. We begin by introducing the definition of the frequency shift, denoted as z.

$$1 + z = \frac{\omega_e}{\omega_d}. \tag{6}$$

Here, ω_e represents the frequency measured by an observer moving with the photon-emitting particle, while ω_d refers to the frequency observed by a distant observer, far from the emission source. One can express them as

$$\omega_e = -k_\mu U^\mu|_e, \qquad \omega_d = -k_\mu U^\mu|_d \tag{7}$$

In this context, $U^\mu = (U^t, U^r, U^\theta, U^\phi)$ denotes the 4-velocity of a particle traveling along a geodesic, while $k^\mu = (k^t, k^r, k^\theta, k^\phi)$ represents the 4-momentum of photons moving along null geodesics, characterized by the condition $k_\mu k^\mu = 0$.

We begin by calculating U^μ and k^μ, which can be derived using the following Euler–Lagrange equations:

$$\frac{\partial \mathcal{L}}{\partial x^\mu} - \frac{d}{dt}\left(\frac{\partial \mathcal{L}}{\partial \dot{x}^\mu}\right) = 0 \tag{8}$$

with Lagrangian $\mathcal{L}$ that can be written as

$$\mathcal{L} = \frac{1}{2} g_{\mu\nu} \dot{x}^\mu \dot{x}^\nu \tag{9}$$

$$\mathcal{L} = \frac{1}{2}(g_{tt}\dot{t}^2 + g_{rr}\dot{r}^2 + g_{\theta\theta}\dot{\theta}^2 + g_{\phi\phi}\dot{\phi}^2). \tag{10}$$

Here, $\dot{x}^\mu = dx^\mu/d\lambda$ and λ is an affine parameter that parameterizes the particle's trajectory. Owing to the presence of spacelike and timelike Killing vectors that correspond to symmetries in the t and ϕ coordinates, the conserved quantities along the geodesics can be expressed as follows:

$$p_t = \frac{\partial \mathcal{L}}{\partial \dot{t}} = g_{tt}\dot{t} = g_{tt}U^t = -E \tag{11}$$

$$p_\phi = \frac{\partial \mathcal{L}}{\partial \dot{\phi}} = g_{tt}\dot{\phi} = g_{\phi\phi}U^\phi = L \tag{12}$$

Then, one can write the expressions for t and ϕ components of the 4-velocity as

$$U^t = -\frac{E}{g_{tt}} = \frac{E}{f(r)}, \qquad U^\phi = \frac{L}{g_{\phi\phi}} = \frac{L}{r^2 \sin^2\theta} \tag{13}$$

Then, with the use of the normalization condition

$$-1 = g_{tt}(U^t)^2 + g_{rr}(U^r)^2 + g_{\theta\theta}(U^\theta)^2 + g_{\phi\phi}(U^\phi)^2\,, \tag{14}$$

one can easily obtain

$$(U^r)^2 + f(r)W_{eff} = 0. \tag{15}$$

Here, W_{eff} corresponds to the effective potential of massive particle emitting electromagnetic radiation and has the following form:

$$W_{eff} = 1 + r^2 U^\theta - \frac{E^2}{f(r)} + \frac{L^2}{r^2 \sin^2\theta}. \tag{16}$$

We now examine the 4-momentum k^μ of photons by utilizing the Lagrangian (10). The constants of motion, which are the energy and the angular momentum perpendicular to the azimuthal direction, are given by

$$E_\gamma = f(r)k^t, \;\; L_\gamma = r^2 \sin^2\theta k^\phi. \tag{17}$$

As a result, the components of the 4-momentum k_t and k_ϕ can be linked to E_γ and L_γ, respectively. We can now reframe the expression for $1+z$ introduced in (7) as

$$1 + z = \frac{(E_\gamma U^t - L_\gamma U^\phi - U^r k^r / f(r) - r^2 U^\theta k^\theta)|e}{(E_\gamma U^t - L_\gamma U^\phi - U^r k^r / f(r) - r^2 U^\theta k^\theta)|_d}. \tag{18}$$

In observational astronomy, frequency shift data are typically expressed through a kinematic frequency shift z_{kin}, defined as $z_{kin} = z - z_c$. Here, z_c represents the central frequency shift, corresponding to the gravitational redshift of a photon emitted by a particle that is stationary along the line extending from the center to a distant observer. This gives

$$1 + z_c = \frac{(E_\gamma U^t)|e}{(E_\gamma U^t)|d} = \frac{U^t_e}{U^t_d}. \tag{19}$$

The expression for z_{kin} becomes

$$z_{kin} = \frac{(U^t - bU^\phi - \frac{1}{E_\gamma f(r)} U^r k^2 - \frac{1}{E_\gamma} r^2 U^\theta k^\theta)|e}{(U^t - bU^\phi - \frac{1}{E_\gamma f(r)} U^r k^2 - \frac{1}{E_\gamma} r^2 U^\theta k^\theta)|d} - \frac{U^t_e}{U^t_d}, \tag{20}$$

where the quantity $b = L\gamma / E_\gamma$ is introduced as the apparent impact parameter of photons. When both E_γ and L_γ remain conserved along null paths from emission to detection, it follows that $b_e = b_d$.

In this study, the focus is on analyzing z_{kin}. For this we calculate the redshift for a photon emitted by an observer moving freely along a circular orbit as observed by a stationary observer at infinity. This configuration is particularly relevant because it models scenarios commonly encountered in astrophysical contexts, such as the emission of radiation from particles in the accretion disks of compact objects, where particles are often assumed to move along circular orbits. The stationary observer at infinity represents a typical approximation for a distant astronomer observing the system, thereby making the results directly applicable to observational studies. Moreover, this setup simplifies the analysis while retaining physical significance, allowing for the isolation of key relativistic effects such as gravitational redshift, Doppler shift, and the interplay between them in curved spacetime. This clarity provides valuable insights into the underlying physics without introducing unnecessary complexities from more general trajectories.

When $U^\theta = 0$ in the equatorial plane, the simplified expression for Equation (20) is

$$z_{kin} = \frac{U_e^t U_d^\phi b_d - U_d^t U_e^\phi b_e}{U_d^t (U_d^t - b_d U_d^\phi)}\,. \tag{21}$$

This equation does not account for gravitational light bending. For this, one would need to calculate $b = b(r_c)$, where r_c is the radius of the photon emitter's circular orbit. For photons emitted on either side of the compact object, where $k_r = 0$ and $k_\theta = 0$, k_t and k_ϕ are defined by (17). From $k_\mu k^\mu = 0$, one obtains

$$b_\pm = \pm\sqrt{-\frac{g_{\phi\phi}}{g_{tt}}} = \pm\frac{r}{\sqrt{f(r)}}. \tag{22}$$

For a distant observer, i.e., when $r \to \infty$, we have $U^r = U^\theta = U^\phi = 0$ and $U^t = 1 = E$. Consequently, Equation (21) simplifies to

$$z_{kin} = -U^\phi b_e. \tag{23}$$

In Equation (22), the impact parameter $b(r)$ and the kinematic frequency shift z_{kin} may have different signs. A redshift ($z_r > 0$) corresponds to an emitter moving away, while a blueshift ($z_b < 0$) indicates an approaching emitter.

In the equatorial plane, the effective potential takes the simple form

$$W_{eff} = 1 + \frac{E^2}{g_{tt}} + \frac{L^2}{g_{\phi\phi}} = 1 - \frac{E^2}{f(r)} + \frac{L^2}{r^2}. \tag{24}$$

For circular orbits, both W_{eff} and its derivative $\frac{dW_{eff}}{dr}$ must vanish. Using these conditions, one can derive general expressions for the constants of motion E^2 and L^2 in any static spherically symmetric spacetime:

$$E^2 = \frac{g_{tt}^2 g'_{\phi\phi}}{g_{tt}g'_{\phi\phi} - g'_{tt}g_{\phi\phi}} = \frac{2f^2(r_c)}{2f(r_c) - r_c f'(r_c)}, \tag{25}$$

$$L^2 = \frac{g_{\phi\phi}^2 g'_{tt}}{g_{tt}g'_{\phi\phi} - g'tt g_{\phi\phi}} = \frac{r_c^3 f'(r_c)}{2f(r_c) - r_c f'(r_c)}. \tag{26}$$

For circular orbit stability, an additional condition $W''_{eff} > 0$ is required. Using Equations (25) and (26), W''_{eff} is expressed as

$$W''_{eff} = -E^2\left[\frac{g''_{tt}g_{tt} - 2(g'_{tt})^2}{g_{tt}^3}\right] - L^2\left[\frac{g''_{\phi\phi}g_{\phi\phi} - 2(g'_{\phi\phi})^2}{g_{\phi\phi}^3}\right] = \frac{g'_{\phi\phi}g''_{tt} - g'_{tt}g''_{\phi\phi}}{g_{tt}g'_{\phi\phi} - g'_{tt}g_{\phi\phi}} + \frac{2g'_{tt}g'_{\phi\phi}}{g_{tt}g_{\phi\phi}} \tag{27}$$

$$= \frac{2[rf(r)f''(r) + 3f(r)f'(r) - 2rf'(r)]^2}{rf(r)[2f(r) - rf'(r)]}. \tag{28}$$

From (13), one can easily derive the expressions for the 4-velocities:

$$U^\phi = \sqrt{\frac{f'(r)}{r(2f(r) - rf'(r))}}, \quad U^t = \sqrt{\frac{2}{2f(r) - rf'(r)}}\,. \tag{29}$$

As a result, the angular velocity of particles in circular orbits can now be expressed as

$$\Omega = \sqrt{-\frac{g'_{tt}}{g'_{\phi\phi}}} = \sqrt{\frac{f'(r)}{2r}}. \tag{30}$$

Using the explicit expressions for U_e^ϕ and b_e, the frequency shift can be written as

$$z = U_e^\phi b_{e_+} = \sqrt{\frac{-g_{\phi\phi} g'_{tt}}{g_{tt}(g'_{\phi\phi} g_{tt} - g_{\phi\phi} g'_{tt})}} = \sqrt{\frac{r_c f'(r_c)}{f(r_c)(2f(r_c) - r_c f'(r_c))}}. \tag{31}$$

This allows us to analyze how the red/blueshifts of light, emitted by particles following circular geodesics at radius r_c, depend on the parameters of the spacetime. Since, for spherically symmetric spacetimes, the redshift and blueshift only differ in sign, further analysis can focus on the positive frequency shift (i.e., redshift).

For the specific spacetime under consideration, the lapse function $f(r)$ is provided in (1). By substituting this function into (31), the radial dependence of the photon frequency shift can be determined for different values of the spacetime parameters as given in Figure 7. In the top-left plot, which is for fixed l and various Q, it is clearly shown that an increase in the electric charge of a black hole reduces the gravitational redshift of photons coming from the vicinity of a black hole. This in turn can be interpreted as follows: In the previous sections, we have seen that an increase in electric charge reduces the overall gravitational field of a black hole so, for weaker gravitational fields, one can expect a smaller shift in frequencies as well. It is also evident that the redshift of photons goes down quickly with the increase in the distance from the central compact object. Similar behavior is presented in the top-right panel of Figure 7, where we fix the electric charge and vary the length factor l. By comparing it with the top-left panel, one can notice that the effect of l is slightly stronger than that of the electric charge of the central black hole in the closer vicinity of a black hole, while in the further distances, its effect becomes weaker than the latter. In the middle-left panel, the density plot of the gravitational redshift of photons is shown in the l–Q parameter space for a fixed radial distance. It can be observed that the gravitational redshift is stronger for smaller values of both spacetime parameters and reaches its maximum for the Schwarzschild case. It is also clearly demonstrated that the redshift value is more sensitive to the electric charge of the black hole compared with the length factor. In the middle-right and bottom panels, the change in the redshift of photons with varying radial coordinates and one spacetime parameter is shown, while keeping the other spacetime parameter fixed. One can ensure from plots that the redshift of photons decreases fast with the increase in the radial distance from the central black hole. They further demonstrate that the variation in redshift is less sensitive to changes in the length factor l compared with the electric charge Q.

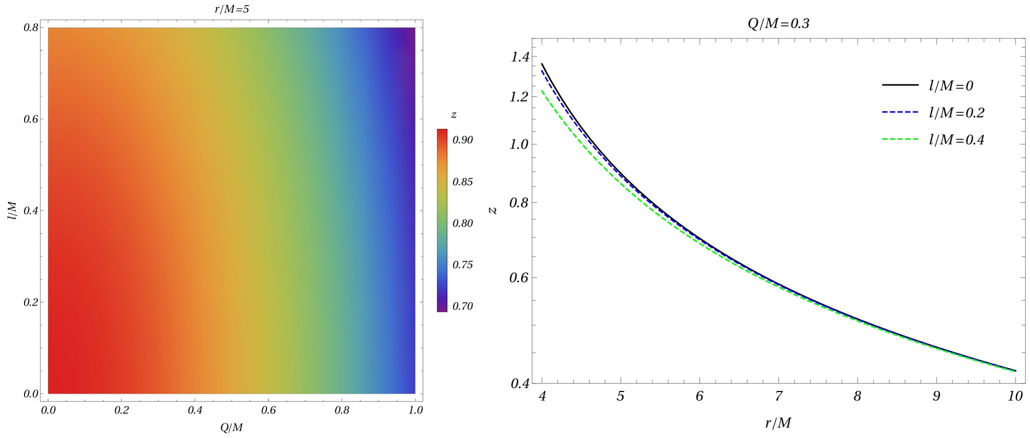

Figure 7. *Cont.*

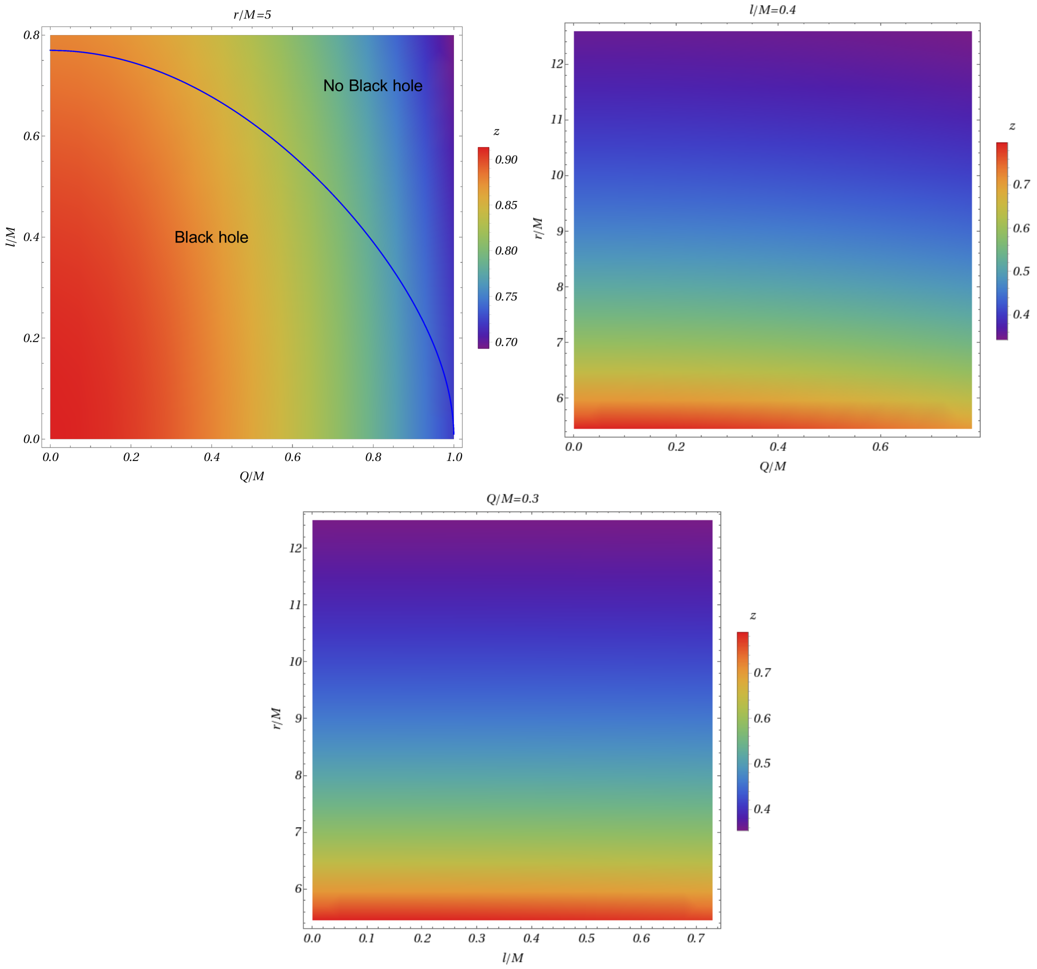

Figure 7. Density Plot version of the results for the dependence of the redshift of photons from the radial coordinate and the spacetime parameters of a charged Hayward black hole.

5. Conclusions

In this study, we explored the behavior of spacetime and photon dynamics around a Hayward black hole with an electric charge. We mapped the regions of spacetime that admit black hole solutions, noting that the presence of the length factor l reduces the maximum allowed electric charge for which a black hole can exist. Without l, the maximum charge aligns with the Reissner–Nordström limit, but this limit decreases as the length factor increases, vanishing at $l/M \simeq 0.77$. The black hole in this spacetime exhibits both inner and outer horizons. As both the electric charge Q and length factor l increase, the outer event horizon shrinks, while the inner horizon expands, indicating a reduction in the size of the black hole's event horizon for higher values of both parameters. The Kretschmann scalar, representing the curvature of spacetime, is strongly dependent on the values of l and Q. Spacetime curvature reaches a maximum when both parameters approach zero, mimicking the behavior of a Schwarzschild black hole. Interestingly, the effects of spacetime parameters inside a black hole strongly depend on the radial coordinate and are not monotonic everywhere. It was also demonstrated that in the presence of the length factor, we always have a regular black hole solution.

The size of the photon sphere, where light can orbit the black hole, decreases as the electric charge of a black hole increases and shifts to smaller radii with larger values of l. However, the influence of l on the photon sphere is less substantial compared with that of the electric charge. By investigating the redshift of photons, we observed that the gravitational redshift of photons is more sensitive to the electric charge than to the length factor. As Q increases, the redshift diminishes, reflecting a weakening of the gravitational field. The redshift also decreases rapidly with increasing distance from the black hole, and while the effect of l is noticeable, it remains weaker than that of Q at further distances.

Overall, the results indicate that both the electric charge and the length factor significantly impact black hole properties, such as horizon structure, spacetime curvature, and photon dynamics. However, the electric charge exerts a more dominant influence, particularly in relation to gravitational redshift and photon behavior. These findings enhance our understanding of black hole solutions in modified gravity frameworks and provide insights into the role of additional spacetime parameters in shaping black hole physics.

Author Contributions: Investigation, B.S., Formal analysis, B.S., Writing—original draft, B.S., B.N., A.A. and B.A., Methodology, B.S., B.N., A.A., M.K. and B.A., Project administration, B.N., A.A., M.K. and B.A., Supervision, B.N., A.A., M.K. and B.A., Writing—review and editing, B.N., A.A., M.K. and B.A. All authors have read and agreed to the published version of the manuscript.

Funding: This research received no external funding.

Data Availability Statement: Not applicable.

Conflicts of Interest: The authors declare no conflicts of interest.

References

1. Penrose, R. Gravitational collapse and space-time singularities. *Phys. Rev. Lett.* **1965**, *14*, 57–59. [CrossRef]
2. Hawking, S. The occurrence of singularities in cosmology. III. Causality and singularities. *Proc. Roy. Soc. Lond. A* **1967**, *300*, 187–201. [CrossRef]
3. Hawking, S.W.; Penrose, R. The Singularities of gravitational collapse and cosmology. *Proc. R. Soc. Lond. A* **1970**, *314*, 529–548. [CrossRef]
4. Iorio, L. Editorial for the Special Issue 100 Years of Chronogeometrodynamics: The Status of the Einstein's Theory of Gravitation in Its Centennial Year. *Universe* **2015**, *1*, 38–81. [CrossRef]
5. Debono, I.; Smoot, G.F. General Relativity and Cosmology: Unsolved Questions and Future Directions. *Universe* **2016**, *2*, 23. [CrossRef]
6. Vishwakarma, R.G. Einstein and Beyond: A Critical Perspective on General Relativity. *Universe* **2016**, *2*, 11. [CrossRef]
7. Beltrán Jiménez, J.; Heisenberg, L.; Koivisto, T.S. The Geometrical Trinity of Gravity. *Universe* **2019**, *5*, 173. [CrossRef]
8. Capozziello, S.; De Bianchi, S.; Battista, E. Avoiding singularities in Lorentzian-Euclidean black holes: The role of atemporality. *Phys. Rev. D* **2024**, *109*, 104060. [CrossRef]
9. Lan, C.; Yang, H.; Guo, Y.; Miao, Y.G. Regular Black Holes: A Short Topic Review. *Int. J. Theor. Phys.* **2023**, *62*, 202. [CrossRef]
10. Battista, E.; Esposito, G. Geodesic motion in Euclidean Schwarzschild geometry. *Eur. Phys. J. C* **2022**, *82*, 1088. [CrossRef]
11. Misyura, M.; Rincon, A.; Vertogradov, V. Non-singular black hole by gravitational decoupling and some thermodynamic properties. *Phys. Dark Univ.* **2024**, *46*, 101717. [CrossRef]
12. Sakharov, A.D. Nachal'naia stadija rasshirenija Vselennoj i vozniknovenije neodnorodnosti raspredelenija veshchestva. *Sov. Phys. JETP* **1966**, *22*, 241.
13. Gliner, E. Algebraic Properties of the Energy-Momentum Tensor and Vacuum-Like States of Matter. *Sov. Phys.-JETP* **1966**, *22*, 378–382.
14. Bardeen, J. Non-singular general relativistic gravitational collapse. In Proceedings of the Conference Proceedings of GR5, Tbilisi, Georgia, 9–16 September 1968; p. 174.
15. Ayón-Beato, E.; García, A. Regular Black Hole in General Relativity Coupled to Nonlinear Electrodynamics. *Phys. Rev. Lett.* **1998**, *80*, 5056–5059. [CrossRef]
16. Ayon-Beato, E.; Garcia, A. Nonsingular charged black hole solution for nonlinear source. *Gen. Rel. Grav.* **1999**, *31*, 629–633. [CrossRef]
17. Ayon-Beato, E.; Garcia, A. The Bardeen model as a nonlinear magnetic monopole. *Phys. Lett. B* **2000**, *493*, 149–152. [CrossRef]
18. Dymnikova, I. Vacuum nonsingular black hole. *Gen. Relativ. Gravit.* **1992**, *24*, 235–242. [CrossRef]
19. Dymnikova, I. Regular electrically charged structures in nonlinear electrodynamics coupled to general relativity. *Class. Quant. Grav.* **2004**, *21*, 4417–4429. [CrossRef]
20. Bronnikov, K.A. Regular magnetic black holes and monopoles from nonlinear electrodynamics. *Phys. Rev. D* **2001**, *63*, 044005. [CrossRef]
21. Bronnikov, K.A.; Fabris, J.C. Regular Phantom Black Holes. *Phys. Rev. Lett.* **2006**, *96*, 251101. [CrossRef]
22. Berej, W.; Matyjasek, J.; Tryniecki, D.; Woronowicz, M. Regular black holes in quadratic gravity. *Gen. Relativ. Gravit.* **2006**, *38*, 885–906. [CrossRef]
23. Burinskii, A.; Hildebrandt, S.R. New type of regular black holes and particlelike solutions from nonlinear electrodynamics. *Phys. Rev. D* **2002**, *65*, 104017. [CrossRef]

24. Ansoldi, S. Spherical black holes with regular center: A Review of existing models including a recent realization with Gaussian sources. *arXiv* **2008**, arXiv:0802.0330.
25. Ashtekar, A.; Bojowald, M. Black hole evaporation: A Paradigm. *Class. Quant. Grav.* **2005**, *22*, 3349–3362. [CrossRef]
26. Hayward, S.A. Formation and Evaporation of Nonsingular Black Holes. *Phys. Rev. Lett.* **2006**, *96*, 031103. [CrossRef]
27. Hakimov, A.; Abdujabbarov, A.; Narzilloev, B. Quantum interference effects in conformal Weyl gravity. *Int. J. Mod. Phys. A* **2017**, *32*, 1750116. [CrossRef]
28. Rayimbaev, J.; Narzilloev, B.; Abdujabbarov, A.; Ahmedov, B. Dynamics of Magnetized and Magnetically Charged Particles around Regular Nonminimal Magnetic Black Holes. *Galaxies* **2021**, *9*, 71. [CrossRef]
29. Narzilloev, B.; Rayimbaev, J.; Abdujabbarov, A.; Ahmedov, B. Regular Bardeen Black Holes in Anti-de Sitter Spacetime versus Kerr Black Holes through Particle Dynamics. *Galaxies* **2021**, *9*, 63. [CrossRef]
30. Narzilloev, B.; Ahmedov, B. Radiation Properties of the Accretion Disk around a Black Hole Surrounded by PFDM. *Symmetry* **2022**, *14*, 1765. [CrossRef]
31. Narzilloev, B.; Ahmedov, B. Observational and Energetic Properties of Astrophysical and Galactic Black Holes. *Symmetry* **2023**, *15*, 293. [CrossRef]
32. Narzilloev, B.; Abdujabbarov, A.; Hakimov, A. Redshift of photons emitted from the accretion disk of a regular black hole surrounded by dark matter. *Int. J. Mod. Phys. A* **2022**, *37*, 2250144. [CrossRef]
33. Mirzaev, T.; Li, S.; Narzilloev, B.; Hussain, I.; Abdujabbarov, A.; Ahmedov, B. Simulated image of the shadow of the Kerr-Newman-NUT-Kiselev black hole in the Rastall gravity with a thin accretion disk. *Eur. Phys. J. Plus* **2023**, *138*, 47. [CrossRef]
34. Narzilloev, B.; Ahmedov, B. The eye of the storm: Optical properties. *Int. J. Mod. Phys. A* **2023**, *38*, 2350026. [CrossRef]
35. Abdulxamidov, F.; Benavides-Gallego, C.A.; Narzilloev, B.; Hussain, I.; Abdujabbarov, A.; Ahmedov, B.; Xu, H. Dynamics of spinning test particles around the Kerr-Newman-NUT black hole with quintessence in the Rastall gravity. *Eur. Phys. J. Plus* **2023**, *138*, 635. [CrossRef]
36. Alibekov, H.; Narzilloev, B.; Abdujabbarov, A.; Ahmedov, B. Frequency Shift of Photons in the Spacetime of Deformed RN BH. *Symmetry* **2023**, *15*, 1414. [CrossRef]
37. Alloqulov, M.; Narzilloev, B.; Hussain, I.; Abdujabbarov, A.; Ahmedov, B. Energetic processes around electromagnetically charged black hole in the Rastall gravity. *Chin. J. Phys.* **2023**, *85*, 302–317. [CrossRef]
38. Narzilloev, B.; Ahmedov, B. Thermal radiation of thin accretion disk around Taub-NUT black hole. *Int. J. Mod. Phys. D* **2023**, *32*, 2350064. [CrossRef]
39. Gao, B.; Deng, X.M. Bound orbits around modified Hayward black holes. *Mod. Phys. Lett. A* **2021**, *36*, 2150237. [CrossRef]
40. Zhao, S.S.; Xie, Y. Strong deflection gravitational lensing by a modified Hayward black hole. *Eur. Phys. J. C* **2017**, *77*, 272. [CrossRef]
41. Hu, J.P.; Zhang, Y.; Shi, L.L.; Duan, P.F. Structure of geodesics in the regular Hayward black hole space-time. *Gen. Relativ. Gravit.* **2018**, *50*, 89. [CrossRef]
42. Amir, M.; Ghosh, S.G. Rotating Hayward's regular black hole as particle accelerator. *J. High Energy Phys.* **2015**, *7*, 15. [CrossRef]
43. Pedraza, O.; López, L.A.; Arceo, R.; Cabrera-Munguia, I. Geodesics of Hayward black hole surrounded by quintessence. *Gen. Relativ. Gravit.* **2021**, *53*, 24. [CrossRef]
44. Abbas, G.; Sabi Ullah, U. Geodesic Study of Regular Hayward Black Hole. *Astrophys. Space Sci.* **2014**, *352*, 769–774. [CrossRef]
45. Kumar, R.; Ghosh, S.G.; Wang, A. Shadow cast and deflection of light by charged rotating regular black holes. *Phys. Rev. D* **2019**, *100*, 124024. [CrossRef]
46. Fabian, A.C.; Iwasawa, K.; Reynolds, C.S.; Young, A.J. Broad Iron Lines in Active Galactic Nuclei. *Publ. Astron. Soc. Pac.* **2000**, *112*, 1145–1161. [CrossRef]
47. Miller, J.M. Relativistic X-ray Lines from the Inner Accretion Disks Around Black Holes. *Ann. Rev. Astron. Astrophys.* **2007**, *45*, 441–479. [CrossRef]
48. Laor, A. Line Profiles from a Disk around a Rotating Black Hole. *Astrophys. J.* **1991**, *376*, 90. [CrossRef]
49. Reynolds, C.S.; Nowak, M.A. Fluorescent iron lines as a probe of astrophysical black hole systems. *Phys. Rep.* **2003**, *377*, 389–466. [CrossRef]
50. Tanaka, Y.; Nandra, K.; Fabian, A.C.; Inoue, H.; Otani, C.; Dotani, T.; Hayashida, K.; Iwasawa, K.; Kii, T.; Kunieda, H.; et al. Gravitationally Redshifted Emission Implying an Accretion Disk and Massive Black Hole in the Active Galaxy MCG:-6-30-15. *Nature* **1995**, *375*, 659. [CrossRef]
51. Brenneman, L.W.; Reynolds, C.S. Constraining Black Hole Spin via X-ray Spectroscopy. *Astrophys. J.* **2006**, *652*, 1028–1043. [CrossRef]
52. Reynolds, C.S. Measuring Black Hole Spin Using X-ray Reflection Spectroscopy. *Space Sci. Rev.* **2014**, *183*, 277–294. [CrossRef]
53. Wilms, J.; Reynolds, C.S.; Begelman, M.C.; Reeves, J.; Molendi, S.; Staubert, R. XMM-EPIC observation of MCG-6-30-15: Direct evidence for the extraction of energy from a spinning black hole? *Mon. Not. R. Astron. Soc.* **2001**, *328*, L27–L31. [CrossRef]
54. García, J.; Dauser, T.; Lohfink, A.; Kallman, T.R.; Steiner, J.F.; McClintock, J.E.; Brenneman, L.; Wilms, J.; Eikmann, W.; Reynolds, C.S.; et al. Improved reflection models of black hole accretion disks: Treating the ionization balance with XSTAR. *Astrophys. J.* **2014**, *782*, 76. [CrossRef]
55. Dovčiak, M.; Karas, V.; Yaqoob, T. KYRLINE: Relativistic line model. *Astrophys. J. Suppl. Ser.* **2004**, *153*, 205–221. [CrossRef]

56. Niedźwiecki, A.; Zdziarski, A.A. X-ray polarization and black hole accretion geometry. *Mon. Not. R. Astron. Soc.* **2008**, *386*, 759–769. [CrossRef]
57. McClintock, J.E.; Narayan, R.; Steiner, J.F. Measuring the spins of stellar-mass black holes. *Class. Quantum Gravity* **2011**, *28*, 114009. [CrossRef]
58. Remillard, R.A.; McClintock, J.E. X-ray properties of black-hole binaries. *Annu. Rev. Astron. Astrophys.* **2006**, *44*, 49–92. [CrossRef]
59. Frolov, V.P. Notes on nonsingular models of black holes. *Phys. Rev. D* **2016**, *94*, 104056. [CrossRef]
60. Herrera-Aguilar, A.; Nucamendi, U. Kerr black hole parameters in terms of the redshift/blueshift of photons emitted by geodesic particles. *Phys. Rev. D* **2015**, *92*, 045024. [CrossRef]